Reversible voltammograms and a Pourbaix diagram for a protein tyrosine radical

Bruce W. Berry[a,b], Melissa C. Martínez-Rivera[a], and Cecilia Tommos[a,b,1]

[a]Graduate Group in Biochemistry and Molecular Biophysics and Department of Biochemistry and Biophysics, 905 Stellar-Chance Laboratories, University of Pennsylvania, Philadelphia, PA 19104-6059; and [b]Department of Biochemistry and Biophysics, Arrhenius Laboratories for Natural Sciences, Stockholm University, SE-106 91 Stockholm, Sweden

Edited by Harry B. Gray, California Institute of Technology, Pasadena, CA, and approved May 1, 2012 (received for review July 25, 2011)

Reversible voltammograms and a voltammetry half-wave potential versus solution pH diagram are described for a protein tyrosine radical. This work required a de novo designed tyrosine-radical protein displaying a unique combination of structural and electrochemical properties. The α_3Y protein is structurally stable across a broad pH range. The redox-active tyrosine Y32 resides in a desolvated and well-structured environment. Y32 gives rise to reversible square-wave and differential pulse voltammograms at alkaline pH. The formal potential of the Y32-O$^\bullet$/Y32-OH redox couple is determined to 918 ± 2 mV versus the normal hydrogen electrode at pH 8.40 ± 0.01. The observation that Y32 gives rise to fully reversible voltammograms translates into an estimated lifetime of ≥30 ms for the Y32-O$^\bullet$ state. This illustrates the range of tyrosine-radical stabilization that a structured protein can offer. Y32 gives rise to quasireversible square-wave and differential pulse voltammograms at acidic pH. These voltammograms represent the Y32 species at the upper edge of the quasirevesible range. The square-wave net potential closely approximates the formal potential of the Y32-O$^\bullet$/Y32-OH redox couple to 1,070 ± 1 mV versus the normal hydrogen electrode at pH 5.52 ± 0.01. The differential pulse voltammetry half-wave potential of the Y32-O$^\bullet$/Y32-OH redox pair is measured between pH 4.7 and 9.0. These results are described and analyzed.

protein voltammetry | proton-coupled electron transfer

Proton-coupled electron transfer (PCET) represents a fundamental component of catalytic and long range radical-transfer processes involving tyrosine radicals (1–4). The thermodynamic and kinetic effects of coupled tyrosine oxidation/reduction and acid/base chemistry at the protein matrix are likely to play a key role in activating the aromatic residue for redox chemistry and for fine tuning its functional properties. This prediction is largely based on three sets of experimental observations that include the thermodynamic properties of aqueous tyrosine (5–7), the hydrogen-bonding properties of the kinetically well-characterized Y_Z and Y_D radicals in photosystem II (PSII) (7–10), and data derived from small-molecule model systems designed to delineate the PCET processes associated with tyrosine/phenol oxidation (4, 11–16). Tyrosine redox chemistry involves three redox couples and two pK_a values. The cation Y-OH$^{\bullet+}$/Y-OH redox pair exists at pH below the pK_a of the oxidized state (pK_{oY}) whereas the tyrosinate Y-O$^\bullet$/Y-O$^-$ couple is observed at pH above the pK_a of the reduced state (pK_{rY}). The neutral tyrosine Y-O$^\bullet$/Y-OH redox couple operates in the pK_{oY} < pH < pK_{rY} region. With pK_{oY} and pK_{rY} values of −2 and 10 for aqueous tyrosine, respectively (5), Y-O$^\bullet$/Y-OH is predicted to be the dominant protein redox pair. Consequently, long-range electron transfer involving protein tyrosine residues is coupled to short-range proton motions between the radical species and the protein matrix. Indeed, studies on Y_Z and Y_D suggested early on that electron and proton transfers associated with tyrosine oxidation/reduction are strongly coupled events (7–9). Studies on solvated small-molecule tyrosine/phenol model systems have reinforced the key observation that local interactions critically determine the redox properties of tyrosine and the PCET mechanism by which the radical state is formed (for a recent review, see ref. 4).

The involvement of tyrosine radicals in biochemical processes has been known for decades. Yet, there is essentially a complete lack of thermodynamic data available for these redox species with published reduction potentials limited to two single-pH estimates (ref. 17 and references therein). This situation underlines the experimental challenges associated with probing the potentials of these highly oxidizing PCET molecules when they reside in a protein environment. Here we present a reduction potential vs. solution pH (Pourbaix) diagram (18) for a protein tyrosine radical. This was made possible by adopting a model protein approach guided by the following criteria. Obtaining a Pourbaix diagram for a *protein* tyrosine radical requires: (*i*) a *protein* system; i.e., a system that exhibits classic protein properties of cooperative structure and stability; (*ii*) that this protein contains a *solvent-sequestered redox-active tyrosine* whose potential can be measured by voltammetry across a broad pH range; (*iii*) that the protein voltammogram reflects a *reversible* electrode process from which *formal* tyrosine potentials can be derived. Here we report voltammetry studies of a de novo designed tyrosine radical model protein that fulfills these unique requirements.

Results and Discussion

α_3Y Is a Well-Structured Protein. The synthetic α_3Y model protein used here is a member of a family of de novo designed radical proteins (2, 17, 19–21). This family is based on a 67-residue scaffold containing three interacting α-helices linked by two glycine loops (Fig. S1). The radical site (position 32) is located in the middle of the central helix and occupied by a tyrosine (to form the α_3Y protein), a tryptophan (α_3W), or a cysteine (α_3C). C32 in α_3C has been used as a chemical link for phenol ligation (22). α_3Y, α_3W, and α_3C exhibit main characteristics associated with well-folded native proteins. They form thermodynamically stable, highly helical structures across a broad pH range. Folding occurs in a reversible, cooperative manner and is driven by the hydrophobic effect. Their tertiary structures are well defined. Importantly, residue 32 resides in a desolvated and highly structured environment. This latter property uniquely separates α_3Y from all previously described tyrosine/phenol radical model systems in which the radical species typically resides in a highly solvated and dynamic environment (4, 23).

α_3Y Voltammetry Control Studies. Cyclic voltammetry (CV) (24) data cannot be obtained for α_3Y due to the poor electrochemical response when using this relatively insensitive technique [see ref. 17 for a comparison in the CV response of a small-molecule

Author contributions: C.T. designed research; B.W.B., M.C.M.-R., and C.T. performed research; B.W.B., M.C.M.-R., and C.T. analyzed data; and C.T. wrote the paper.

The authors declare no conflict of interest.

This article is a PNAS Direct Submission.

[1]To whom correspondence should be addressed. E-mail: tommos@mail.med.upenn.edu.

This article contains supporting information online at www.pnas.org/lookup/suppl/doi:10.1073/pnas.1112057109/-/DCSupplemental.

tyrosine system and α_3Y]. Differential pulse voltammetry (DPV) (24, 25) has better sensitivity than CV and generates a well-defined Faradaic response from α_3Y at both acidic and alkaline conditions. Site-directed mutagenesis unambiguously assigned the observed current to Y32 and showed that the protein scaffold itself is redox inert to at least 1.3 V vs. NHE (17, 22). Examples of raw and background-corrected differential pulse voltammograms, details regarding data processing, and error analyses are provided in *SI Text*. To prove that α_3Y is an electrochemically reversible system we employ the similarly sensitivity technique square-wave voltammetry (SWV) (24, 26, 27). In SWV, the applied potential is stepped progressively in fixed increments, and at each increment, a forward (in this study, oxidative) potential pulse is applied followed by a reverse (reductive) pulse. This generates a forward (I_{for}), a reverse (I_{rev}), and a net ($I_{net} = I_{for} - I_{rev}$) voltammogram. The time between sampling I_{for} and I_{rev} is set by the pulse width (t_p), which is determined by the square-wave frequency ($f = 1/2t_p$). The forward and reverse square-wave voltammograms resemble a cyclic voltammogram and can be used to assess the reversibility of the electrode process (26, 27). For a reversible electrode process, the peak potential of the net current (E_{net}) equals the voltammetry half-wave potential ($E_{1/2}$). Typically, the half-wave potential closely approximates the formal potential ($E^{0'}$). For a diffusion-controlled reversible redox system, $E_{1/2}$ equals $E^{0'}$ when the ratio of the diffusion coefficients of the reduced and oxidized species equals unity (24).

DPV conducted with a glassy carbon (GC) working electrode generates α_3Y voltammograms with good signal-to-noise ratio (S/N) (17) (Fig. S2). In contrast, SWV in combination with a GC electrode generates α_3Y voltammograms with significant lower S/N and this approach was not perused beyond a preliminary assessment. A series of control measurements were conducted to refine a pyrolytic graphite "edge" (PGE) electrode system for a SWV analysis of the α_3Y electrode process. Fig. S3 summarizes experiments conducted to optimize sample conditions (Fig. S3 *A* and *B*) and to determine whether α_3Y gives rise to diffusion-controlled or surface-confined electrode kinetics (Fig. S3*D*). Fig. S4 displays typical raw and background-corrected α_3Y square-wave voltammograms collected at optimized sample conditions and provides details regarding data processing and analyses. Finally, Fig. S5 illustrates the reproducibility observed between data replicates and independent SWV measurements. The main conclusions from the data displayed in Figs. S2–S5 are summarized below and we refer to the *SI Text* for further details. (*i*) SWV samples were optimized at 20–100 μM α_3Y in 20 mM sodium acetate, 20 mM potassium phosphate, 20 mM sodium borate (APB buffer), and 80–140 mM KCl. The S/N of the α_3Y Faradaic current decreases above and below the 20–100 μM protein concentration range. The α_3Y peak potential is independent of the KCl concentration above 10 mM KCl at alkaline pH (pH 8.4) and above 60 mM KCl at acidic pH (pH 5.5). The S/N of the α_3Y voltammogram declines as the KCl concentration rises and accurate determination of peak amplitudes and potentials becomes increasingly difficult above 140 mM KCl. Based on these results, subsequent SWV studies were conducted at 80 μM α_3Y dissolved in a 20 mM APB, 80 mM KCl buffer. (*ii*) The SWV net potential (E_{net}) and the DPV half-wave potential ($E_{1/2}$) are displayed as a function of the α_3Y concentration in Fig. S3 *B* and *C*, respectively. The SWV and DPV measurements were conducted using a PGE and GC electrode, respectively, and the α_3Y concentration series was collected at both acidic and alkaline pH. A very weak to no correlation ($\delta(E_{net}$ or $E_{1/2})/\delta\log[\alpha_3Y] \leq -5.9 \pm 2.6$ mV per decade) is observed for both electrode systems. We conclude that there are no distorting protein/working electrode surface interactions (such as self-inhibition, e.g., ref. 28) present at any conditions used in this report. (*iii*) Voltammograms were recorded at large SW pulse amplitudes to investigate the kinetic characteristics of α_3Y on the PGE electrode (27, 29) (Fig. S3*D*). The observed response is consistent with diffusion-controlled electrode kinetics at both acidic and alkaline pH. (*iv*) The reproducibility in $E_{1/2}$ obtained with the DPV/GC system is ±3 mV for data replicates (Fig. S2 *A* and *D–F*) and ±4 mV for independent measurements (Fig. S2*I*). The reproducibility in E_{net} observed for the SWV/PGE system is ±3 mV for data replicates (Fig. S5 *A–F*) and ±3 mV for independent measurements (Fig. S5 *G–I*). After correcting for small differences in pH, we find no significant difference (5 ± 5 mV) in the α_3Y DPV $E_{1/2}$ value obtained using a GC electrode (Figs. S2 and S3*C*) relative to a PGE electrode (Fig. S3*A*). This concludes the description of control experiments done in preparation for a SWV analysis of the α_3Y electrode process and obtaining a Pourbaix diagram for the tyrosine radical protein.

α_3Y Gives Rise to Reversible Voltammograms. Voltammetry measurements on α_3Y are expected to follow an EC mechanism where "E" represents the electrode reactions (electron and proton transfers associated with the electrode-driven oxidation/reduction of Y32) and "C" represents coupled chemical reactions (i.e., side reactions of the formed Y32-O$^\bullet$ radical). The kinetic and thermodynamic properties of both the E and C processes will influence the observed voltammogram (26, 27, 30–32). In SWV the time between the oxidative and the reductive pulse is set by the SW frequency, which has a practical range of 8–2,000 Hz (t_p 62.5 ms–250 μs). This predicts that for an EC system with a very long-lived radical (i.e., $t_{1/2}$ on the tens of milliseconds time scale), the SW frequency can be set to outcompete the follow-up chemical reaction(s). This would generate voltammograms with properties that only reflect the E process. Remarkably, the protein environment stabilizes the Y32-O$^\bullet$ radical into the required time frame such that voltammograms representing a fully reversible electrode process could be obtained. This is shown below.

α_3Y square-wave voltammograms were recorded using a frequency ranging from 30 Hz (t_p 16.7 ms) to 960 Hz (t_p 521 μs). The three top boxes in Fig. 1 display voltammograms from this data series. Background-corrected forward and reverse square-wave voltammograms collected at 190 Hz (t_p 2.63 ms), 540 Hz (t_p 926 μs), and 750 Hz (t_p 667 μs) are shown in Fig. 1 *A–C*, respectively. Fig. S4 illustrates the quality of the raw voltammograms from this data series and describes methods used for background corrections and data analyses. The key results from the SW frequency series are summarized in Fig. 1 *D* and *E*. Fig. 1*D* shows the change in the peak potentials as a function of the SW frequency. Importantly, the net peak potential (E_{net}) and the peak potentials of the forward (E_{for}) and reverse (E_{rev}) currents become independent of the SW frequency at 750 Hz (Fig. 1*D*). This is a hallmark characteristic of a fully reversible electrode process (26, 27). We further observe that I_{for}/I_{rev} declines from 1.71 ± 0.14 at 30 Hz and reaches a limiting value of 1.01 ± 0.02 for the 750 – 960 Hz range (Fig. 1*E*). Whereas $E_{for} - E_{rev}$ varies between -14 ± 1 and -8 ± 2 in the quasireversible range (30–540 Hz), the effects on E_{net} remain small with a change of 8 ± 2 mV between 30 and 120 Hz and only 4 ± 2 mV for the 120–960 Hz range (Fig. 1*D*). E_{net} equals 918 ± 2 mV vs. NHE for the 750–960 Hz range and represents the formal potential ($E^{0'}$) of the Y32-O$^\bullet$/Y32-OH redox couple at pH 8.40 ± 0.01. This statement assumes that the diffusion coefficient of α_3Y does not change as a function of the protein redox state. The diffusion coefficient of reduced α_3Y was determined to be $1.47 \pm 0.01 \times 10^{-6}$ cm^2 s^{-1} by pulsed field gradient NMR experiments (33) (Fig. S6). This value is typical for a small soluble protein and is not likely to change significantly as Y32 loses an electron and a proton.

The observation that Y32 gives rise to a fully reversible voltammogram means that the radical state is stable on the time scale of the electrochemical oxidation/reduction reactions. Theoretical treatments for EC systems where "E" represents a diffusion-

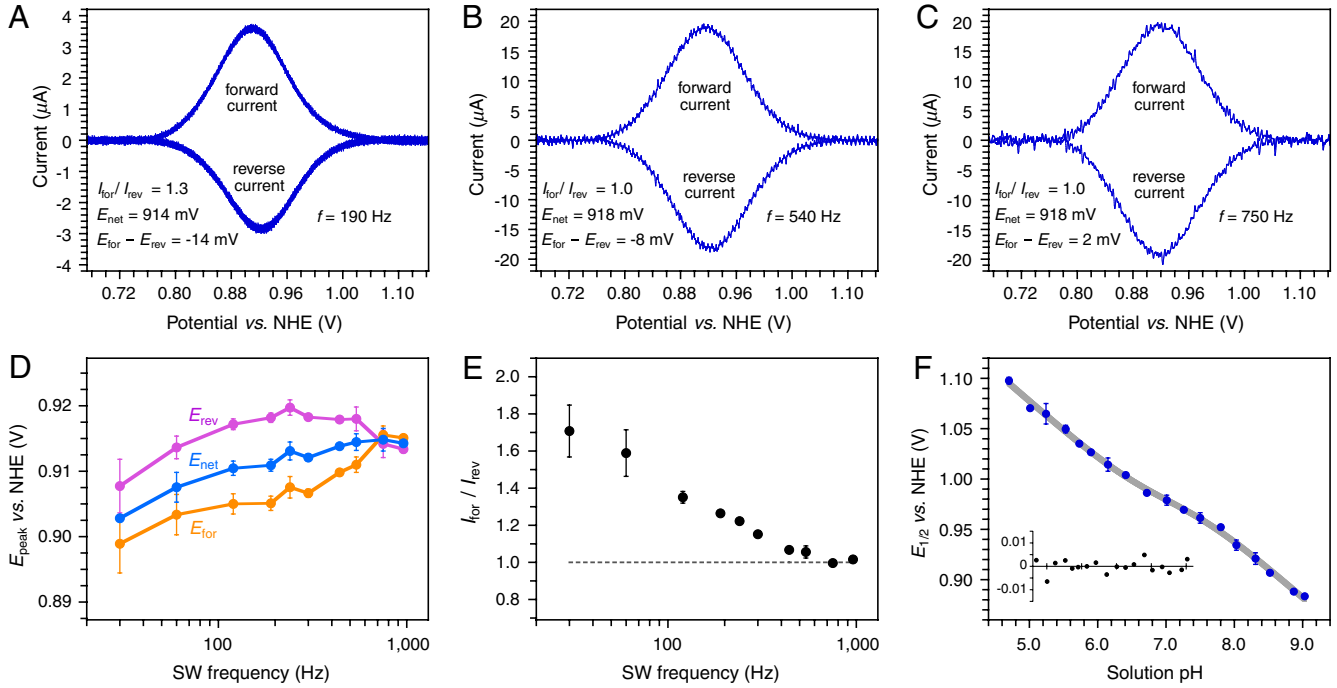

Fig. 1. α_3Y forward (oxidation) and reverse (reduction) square-wave voltammograms obtained at pH 8.40 ± 0.01 and using a SW frequency of (*A*) 190 Hz (t_p 2.6 ms), (*B*) 540 Hz (t_p 926 μs), and (*C*) 750 Hz (t_p 667 μs). These voltammograms form part of a SW frequency series spanning from 30 Hz (t_p 16.7 ms) to 960 Hz (t_p 521 μs). (*D*) describes the change in the peak potential of the net (E_{net}), forward (E_{for}), and reverse (E_{rev}) currents as a function of the SW frequency. *E* plots the ratio of the peak currents of the forward (I_{for}) and reverse (I_{rev}) components as a function of the SW frequency. SWV settings: 80 μM α_3Y in 20 mM APB, 80 mM KCl, pH 8.40 ± 0.01; PGE working electrode, temperature 25 °C, step potential 0.15 mV, SW pulse amplitude 25 mV. (*F*) α_3Y differential pulse half-wave potential ($E_{1/2}$) of as a function of pH. The solid gray line represents a nonlinear regression curve fit to Eq. **1**. The insert displays the corresponding fitting residuals. DPV settings: 200 μM α_3Y in 10 mM APB, 100 mM KCl, GC working electrode, temperature 23 °C, interval time 0.1 s, step potential 1.95 mV, scan rate 19.5 mV s^{-1}, modulation time 2 ms, modulation amplitude 25 mV.

controlled reversible electrode process and "C" is a coupled chemical reaction have been described for SWV (30, 31). They predict that the influence of the coupled chemical reaction on E_{net} approaches zero when $\log(2t_p k_{EC}) \leq -1.5$. This predicts that rate constants (k_{EC}) associated with Y32-O• side reactions are $\leq$24 s^{-1}, which, in turn, translates into a radical lifetime of $\geq$30 ms. The well-structured protein environment of the Y32 site clearly suppresses radical side reactions with a remarkable efficiently. Possible side reactions include intermolecular radical-radical and radical-protein reactions as well as intramolecular radical-protein reactions. For example, for freely solvated tyrosine the oxidized species rapidly dimerizes ($4–8 \times 10^8$ M^{-1} s^{-1}) to form C_{ortho}-C_{ortho} and C_{ortho}-O dityrosine as the major and minor products, respectively. Intermolecular radical reactions are not expected to occur for the Y32 system to any significant extent. The Y32 site is located inside the protein, and the global stability of α_3Y predicts that only 0.2% of the protein population is unfolded at any given time (17, 19). The absence of intermolecular side reactions is consistent with the insensitivity in the SWV E_{net} (190 Hz; Fig. S3*B*) and DPV $E_{1/2}$ (Fig. S3*C*) potentials to the protein concentration. As a comparison, aqueous *N*-acetyl-tyrosinamide (NAYA) displays a $\delta E_{1/2}/\delta \log[NAYA]$ dependence of −30 ± 3 mV per decade (Fig. S3*C*) reflecting rapid intermolecular radical reactions. Intramolecular radical-protein reactions could occur in α_3Y. ^{1}H-^{1}H nuclear Overhauser effect spectroscopy (NOESY) spectra show that the Y32 site is comprised of numerous aliphatic C-H groups (17, 19). This suggests that hydrogen-atom abstraction from C-H bonds may represent the dominant route for chemical reduction of Y32-O•. These reactions typically exhibit low rate constants (34). They are also predicted to be pH independent, which becomes important for the interpretation of the Pourbaix diagram derived for α_3Y (*vide infra*).

Collecting SW voltammograms in the pH 5.5 region was more challenging for two reasons. The Faradaic current decreases at lower pH (e.g., compare Fig. 1 *A* and *B* to Fig. 2 *A* and *B*) whereas the Y32 potential increases to above +1.0 V vs. NHE. This makes background currents (arising from the aqueous solvent and the electrode itself) more pronounced. Nonetheless, voltammograms of satisfactory S/N were collected at 190 and 540 Hz. Background-corrected forward and reverse voltammograms obtained at pH 5.52 ± 0.01 are shown in Fig. 2. Examples of raw data triplicates of the net, forward, and reverse components are shown in Fig. S5 *D–F*, respectively. The properties of the low-pH voltammograms exhibit the same overall frequency dependence as the high-pH data. I_{for}/I_{rev} drops from 1.44 ± 0.03 (190 Hz) to 1.15 ± 0.01 (540 Hz), $E_{for} - E_{rev}$ decreases from −11 ± 1 mV (190 Hz) to −3 ± 1 mV (540 Hz), and a minor change from 1,066 ± 2 mV (190 Hz) to 1,070 ± 1 mV (540 Hz) is observed for E_{net}. These characteristics strongly suggest that the 540 Hz voltammogram represents the Y32 system at the upper edge of the quasireversible range and that E_{net} (pH 5.52; 540 Hz) deviates from $E^{0'}$ (pH 5.52) by a few mV at most (27). We therefore conclude that 1,070 ± 1 mV vs. NHE closely approximates the formal potential of the Y32-O•/Y32-OH redox couple at pH 5.52 ± 0.01.

Pourbaix Diagram of α_3Y. Fig. 1*F* shows the DPV $E_{1/2}$ potential of α_3Y as a function of the solution pH. The α_3Y potential displays a nonlinear relationship across the investigated 4.7–9.0 pH range. The SWV analysis described above provides an explanation to the observed pH dependence. The formal potential of the Y32-O•/Y32-OH redox couple is 918 ± 2 mV at pH 8.40 ± 0.01. From the $E_{1/2}$ vs. pH plot in Fig. 1*F* we extract a potential of 916 ± 3 mV at pH 8.40. There is no significant difference between the formal potential of the Y32-O•/Y32-OH redox couple as determined by SWV and the $E_{1/2}$ value derived by DPV. Consequently, the α_3Y SW voltammogram (pH 8.40; $\geq$750 Hz)

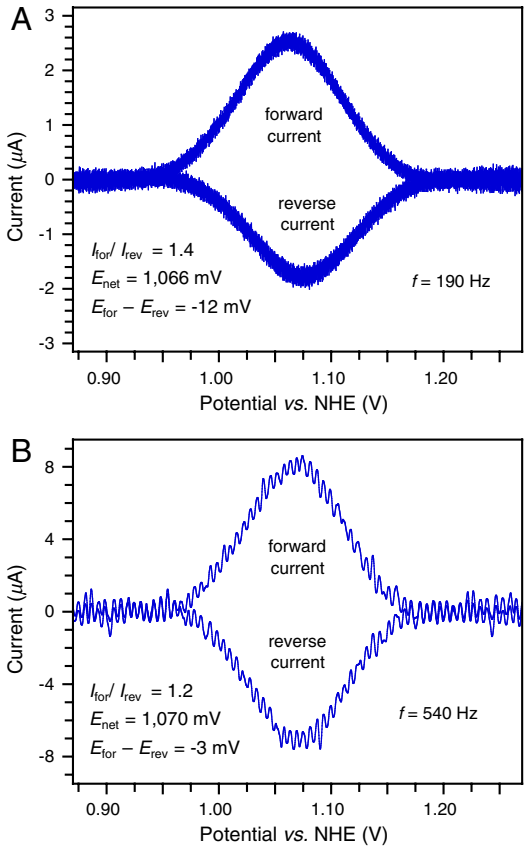

Fig. 2. α_3Y forward (oxidation) and reverse (reduction) square-wave voltammograms obtained at 5.52 ± 0.01 and using a SW frequency of (*A*) 190 Hz (t_p 2.6 ms) and (*B*) 540 Hz (t_p 926 μs). SWV settings: 80 μM α_3Y in 20 mM APB, 80 mM KCl, pH 5.52 ± 0.01; PGE working electrode, temperature 25 °C, step potential 0.15 mV, SW pulse amplitude 25 mV.

and the DP voltammogram (pH 8.40) are both derived from a fully reversible electrode process.

The DPV $E_{1/2}$ (pH 5.52) value is 22 ± 3 mV lower relative to the 1,070 ± 1 mV (pH 5.52; 540 Hz) value determined by SWV. Tyrosine oxidation is a PCET event, that is, the kinetic and thermodynamic properties of the electron transfer depend on the position of one (or several protons) at any given time (35). It is well established that the hydrogen-bonding properties of the phenol OH group and the characteristics of the base accepting the phenolic proton upon oxidation strongly influence the oxidation mechanism and associated PCET rate constants. The small 22 mV shift in the DPV $E_{1/2}$ potential relative to the SWV E_{net} value is likely to arise from coupled protonic reactions lowering the Y32/electrode electron-transfer rate into the quasireversible regime for the DPV experiment. The alternative explanation is that k_{EC} increases as the pH decreases and makes the system quasireversible. We favor the former explanation because the effects of coupled protonic reaction are expected to be highly sensitive to the pH (e.g., by pH-induced changes in the hydrogen-bonding properties of Y32) whereas k_{EC} is not (*vide supra*).

Based on the discussion presented above, the α_3Y Pourbaix diagram is modeled by (36):

$$E_{1/2} = E_{1/2}(\text{pH } 0) + \frac{RT}{nF}\ln\left(\frac{[H^+]^2 + K_{rB}[H^+] + K_{rB}K_{rY32}}{([H^+] + K_{oB})}\right), \quad [1]$$

where $E_{1/2}$(pH 0) is the half-wave potential at pH 0 (V); K_{rY32} is the acid dissociation constant of Y32 in its reduced state ($pK_{app} = 11.3$, see ref. 17); K_{rB} and K_{oB} represent apparent acid dissociation constants (K_{app}) of a protein residue *B* when Y32 is in its reduced and oxidized state, respectively; *n* is the number of electron equivalents required to convert one mol of oxidant to one mol of reductant; *T* is the temperature (296 K); *R* is the gas constant (8.314 J mol^{-1} K^{-1}); and *F* is the Faraday constant (96.485 kJ V^{-1} mol^{-1}). Eq. **1** was fitted to the α_3Y Pourbaix diagram with the following results: $E_{1/2}$(pH 0) = 1.37 ± 0.02 V, ln(10)RT/*n*F = 59 ± 5 mV, $pK_{rB} = 6.7 \pm 0.2$, and $pK_{oB} = 7.4 \pm 0.2$. The fitted line is displayed in gray in Fig. 1*F* and the fitting residuals are shown in the *Inset*. In this model, Y32 is thermodynamically coupled to a residue *B* in the protein matrix. Residue *B* is protonated at low pH and unavailable to participate in the protonic reactions associated with the oxidation of Y32. As the pH increases and approaches the pK_{rB} range, residue *B* deprotonates and now becomes available to participate in the PCET reactions associated with Y32 oxidation. The redox-induced shift in the pK_a of residue *B* gives rise to the nonlinearity of the Pourbaix diagram describing the pH dependence of the Y32-O$^\bullet$/Y32-OH redox couple.

Conclusions

This report describes three important experimental results. (*i*) Square-wave and differential pulse voltammograms representing a reversible electrode process have been obtained for a protein tyrosine radical. This represents a unique experimental demonstration of obtaining a formal potential for a protein Y-O$^\bullet$/Y-OH redox pair. (*ii*) The observation of reversible voltammograms translates into an estimated lifetime for the tyrosine radical of ≥30 ms. This is a remarkably long lifetime for a phenol-based radical and illustrates that the protein environment can stabilize the Y32-O$^\bullet$ state by inhibiting deleterious radical side reactions. (*iii*) The first Pourbaix diagram for a protein tyrosine radical is described and analyzed. These results represent a significant advance that is long overdue considering that these important protein redox species were identified as early as 1977 (37). The historically prohibitive challenges associated with obtaining thermodynamic information for protein tyrosine radicals stem from the fact that electrochemical measurements must be performed at the very upper edge of the biological redox scale. Moreover, voltammetry on phenols typically follows an EC mechanism where the electrochemical reduction of the radical state is outcompeted by the coupled chemical reaction. This gives rise to irreversible voltammograms from which $E_{1/2}$ potentials cannot be derived without independent information on the rate of the chemical follow-up reaction. Finally, the voltammetry measurements must be conducted in a pH-stable protein background and be sensitive to interactions at the radical site to generate a meaningful Pourbaix diagram for this PCET cofactor. These experimental barriers have been successfully overcome by the α_3Y system.

The recently published high-resolution crystal structure of PSII provides a striking example as to why it is vital to understand the details associated with tyrosine-mediated PCET processes in nature. Seventeen years ago, Gerald T. Babcock and co-workers proposed a model for photosynthetic water oxidation in which PCET at the level of Y_Z provides the key mechanism by which protons formed during the water-splitting process are transported from the active site to the thylakoid lumen (38, 39). This hypothesis broke significantly with the contemporary metal-centered view of photosynthetic water oxidation as it proposed a mechanistically essential PCET function for the tyrosine rather than a traditional ET role in which Y_Z forms a simple link in an electron-transfer chain. The hypothesis of directional proton transfer driven by the Y_Z redox cycle gave rise to two core structural predictions: That Y_Z is in hydrogen-bonding contact with substrate molecules ligated to the metal cluster and that there is a proton exit channel from the tyrosine via its hydrogen-bonding partner D1-H190 to the thylakoid lumen. The recent 1.9 Å resolution

crystal structure of PSII shows features remarkably consistent with these predictions (10). In light of the new PSII structure, a straightforward refinement of the 1995 hypothesis is to propose a "global" reprotonation of the Y_Z radical upon reduction with a proton from the extended hydrogen-bonding network connecting the metal/substrate/Y_Z molecules. This would allow directional PCET at the Y_Z site as originally proposed but remove the requirement of direct hydrogen-atom transfer from metal-ligated substrate to the Y_Z radical. Overall, the intriguing structural properties of the PSII active site will undoubtedly spark an even more intense interest in the amazing chemistry performed by protein tyrosine radicals.

Materials and Methods

Differential pulse and square-wave voltammetry measurements were performed using an Autolab PGSTAT12 potentiostat equipped with a three-electrode glass cell containing a GC or a PGE working electrode. The working electrode was carefully polished between each measurement. All samples were prepared using ultra-pure chemicals and the measurements made under an argon atmosphere. NMR spectra were collected using a 500 MHz Bruker Advance III spectrometer fitted with a cryo probe. Details regarding electrode preparations, voltammetry setup and measurements, data processing, and data analyses can be found in the *SI Text*.

ACKNOWLEDGMENTS. Funding was provided by National Institutes of Health (NIH) Grant GM079190 and by NIH predoctoral fellowship GM096756 to M.C.M.R.

1. Stubbe J, Nocera DG, Yee CS, Chang MCY (2003) Radical initiation in the class I ribonucleotide reductase: Long-range proton-coupled electron transfer? *Chem Rev* 103:2167–2201.
2. Hoganson CW, Tommos C (2004) The function and characteristics of tyrosyl radical cofactors. *Biochim Biophys Acta* 1655:116–122.
3. Reece SY, Hodgkiss JM, Stubbe J, Nocera DG (2006) Proton-coupled electron transfer: The mechanistic underpinning for radical transport and catalysis in biology. *Phil Trans R Soc B* 1472:1351–1364.
4. Dempsey JL, Winkler JR, Gray HB (2010) Proton-coupled electron flow in protein redox machines. *Chem Rev* 110:7024–7039.
5. Dixon WT, Murphy D (1976) Determination of the acidity constants of some phenol radical cations by means of electron spin resonance. *J Chem Soc Faraday Trans II* 72:1221–1230.
6. Harriman A (1987) Further comments on the redox properties of tryptophan and tyrosine. *J Phys Chem* 91:6102–6104.
7. Tommos C, Babcock GT (2000) Proton and hydrogen currents in photosynthetic water oxidation. *Biochim Biophys Acta* 1458:199–219.
8. Hays A-MA, Vassiliev IR, Golbeck JH, Debus RJ (1999) Role of D1-His190 in the proton-coupled oxidation of tyrosine Y_Z in manganese-depleted photosystem II. *Biochemistry* 38:11851–11865.
9. Tommos C (2002) Electron, proton and hydrogen-atom transfer in photosynthetic water oxidation. *Phil Trans R Soc B* 357:1383–1394.
10. Umena Y, Kawakami K, Shen J-R, Kamiya N (2011) Crystal structure of oxygen-evolving photosystem II at a resolution of 1.9 Å. *Nature* 473:55–60.
11. Sjödin M, Styring S, Åkemark B, Sun L, Hammarström L (2000) Proton-coupled electron transfer from tyrosine in a tyrosine-ruthenium-tris-bipyridine complex: Comparison with tyrosine$_Z$ oxidation in photosystem II. *J Am Chem Soc* 122:3932–3936.
12. Mayer JM (2004) Proton-coupled electron transfer: A reaction chemist's view. *Annu Rev Phys Chem* 55:363–90.
13. Huynh MHV, Meyer TJ (2007) Proton-coupled electron transfer. *Chem Rev* 107: 5004–5064.
14. Reece SY, Nocera DG (2009) Proton-coupled electron transfer in biology: Results from synergistic studies in natural and model system. *Annu Rev Biochem* 78:673–699.
15. Costentin C, Robert M, Savéant J-M (2010) Concerted proton-electron transfers: Electrochemical and related approaches. *Acc Chem Res* 43:1019–1029.
16. Warren JJ, Tronic TA, Mayer JM (2010) Thermochemistry of proton-coupled electron transfer reagents and its implications. *Chem Rev* 110:6961–7001.
17. Martínez-Rivera MC, Berry BW, Valentine KG, Westerlund K, Hay S, Tommos C (2011) Electrochemical and structural properties of a protein system designed to generate tyrosine Pourbaix diagrams. *J Am Chem Soc* 133:17786–17795.
18. Pourbaix M (1974) *Atlas of Electrochemical Equilibria in Aqueous Solutions* (National Association of Corrosion Engineers, Houston, TX), 2nd English Ed.
19. Tommos C, Skalicky JJ, Pilloud DL, Wand AJ, Dutton PL (1999) *De novo* proteins as models of radical enzymes. *Biochemistry* 38:9495–9507.
20. Dai Q-H, et al. (2002) Structure of a *de novo* designed protein model of radical enzymes. *J Am Chem Soc* 124:10952–10953.
21. Westerlund K, Berry BW, Privett HK, Tommos C (2005) Exploring amino-acid radical chemistry: Protein engineering and de novo design. *Biochim Biophys Acta* 1707:103–116.
22. Hay S, Westerlund K, Tommos C (2005) Moving a phenol hydroxyl group from the surface to the interior of a protein: Effects on the phenol potential and pK_A. *Biochemistry* 44:11891–11902.
23. Sibert RS, Josowicz M, Barry BA (2010) Control of proton and electron transfer in *de novo* designed, biomimetic hairpins. *Am Chem Soc Chem Biol* 5:1157–1168.
24. Bard AJ, Faulkner LR (2001) *Electrochemical Methods: Fundamentals and Applications* (John Wiley & Sons, Inc., New York), 2nd Ed.
25. Parry EP, Osteryoung RA (1965) Evaluation of analytical pulse polarography. *Anal Chem* 37:1634–1637.
26. Osteryoung J, O'Dea JJ (1986) Square-wave voltammetry. *Electroanalytical Chemistry*, ed AJ Bard (Marcel Dekker, New York), Vol 5, pp 209–308.
27. Mirčeski V, Komorsky-Lovrić Š, Lovrić M (2007) Square-wave voltammetry: Theory and applications. *Monographs in Electrochemistry*, ed F Scholz (Springer-Verlag, Berlin).
28. Costentin C, Louault C, Robert M, Savéant J-M (2009) The electrochemical approach to concerted proton-electron transfers in the oxidation of phenols in water. *Proc Natl Acad Sci USA* 106:18143–18148.
29. Jeuken LJC, McEvoy JP, Armstrong FA (2002) Insights into gated electron-transfer kinetics at the electrode-protein interface: A square wave voltammetry study of the blue copper protein azurin. *J Phys Chem B* 106:2304–2313.
30. O'Dea JJ, Osteryoung J, Osteryoung RA (1981) Theory of square wave voltammetry for kinetic systems. *Anal Chem* 53:695–701.
31. Miles AB, Compton RG (2000) Simulation of square-wave voltammetry: EC and ECE electrode processes. *J Phys Chem B* 104:5331–5342.
32. Garay F, Milivoj Lovrić M (2002) Square-wave voltammetry of quasi-reversible electrode processes with coupled homogeneous chemical reactions. *J Electroanal Chem* 518:91–102.
33. Zheng G, Prince WS (2009) Simultaneous convection compensation and solvent suppression in biomolecular NMR diffusion experiments. *J Biomol NMR* 45:295–299.
34. Mahoney LR, DaRooge MA (1975) Kinetic behavior and thermochemical properties of phenoxy radical. *J Am Chem Soc* 97:4722–4731.
35. Hammes-Schiffer S, Stuchebrukhov AA (2010) Theory of coupled electron and proton transfer reactions. *Chem Rev* 110:6939–6960.
36. Clarke WM (1960) *Oxidation-Reduction Potentials of Organic Systems* (The Williams & Wilkins Company, Waverly Press Inc., Baltimore, MD).
37. Sjöberg B-M, Reichard P, Gräslund A, Ehrenberg A (1977) Nature of free-radical in ribonucleotide reductase from escherichia-coli. *J Biol Chem* 252:536–541.
38. Tommos C, Tang X-S, Warncke K, Hoganson CW, Styring S, McCracken J, Diner BA, Babcock GT (1995) Spin-density distribution, conformation, and hydrogen bonding of the redox-active tyrosine Y_Z in photosystem II from multiple electron magnetic-resonance spectroscopies: Implication for photosynthetic oxygen evolution. *J Am Chem Soc* 117:10325–10335.
39. Hoganson CW, Lydakis-Simantiris N, Tang X-S, Tommos C, Warncke K, Babcock GT, Diner BA, McCracken J, Styring S (1995) A hydrogen-atom abstraction model for the function of Y_Z in photosynthetic oxygen evolution. *Photosynth Res* 46:177–184.